Applied Thermal Engineering 262 (2025) 125216

Contents lists available at ScienceDirect

Applied Thermal Engineering

journal homepage: www.elsevier.com/locate/apthermeng

Research Paper

Numerical investigation of fin geometries on the effectiveness of passive, phase-change material –based thermal management systems for lithium-ion batteries

M. Ismail [a], J.R. Panter [b], S. Landini [b,*]

[a] Department of Renewable Energy Engineering, Amman Arab University, Amman, Jordan
[b] School of Engineering, Mathematics and Physics, University of East Anglia, Norwich NR4 7TJ, United Kingdom

ARTICLE INFO

Keywords:
Li-Ion batteries
Thermal management systems
Phase change materials
Latent heat
Iso-thermalisation
Design criteria

ABSTRACT

Lithium-ion battery (LIB) packs serve as the primary energy storage solution for electric vehicles (EVs), but suffer from degraded performance under non-uniform and sub-optimal operating temperatures. Passive Thermal Management Systems (TMS) based on solid–liquid Phase Change Materials (PCMs) exhibit significant potential, however PCMs' low thermal conductivity has limited their application. Integrating fins to improve heat transfer has been proposed, but there remains a lack of knowledge regarding how the system size and discharge time scale affects thermal performance with differing fin geometries. Here, a numerical model is developed using Ansys Fluent and validated to examine the time-resolved TMS performance with differing fin geometries under thermal loading and resting conditions. Two system scales are examined, with dimensions of the order of either 10 mm or 100 mm. For small-scale systems, fins offer no meaningful improvement compared to PCM alone: the best-performing fin geometry only reduces the maximum cell temperature by 0.2 °C at the end of a 720 s (5C) discharge. However, for the large-scale system, the performance depends strongly on the discharge duration. Of all geometries, 9 vertical fins are best performing at 480 s of discharge (38.3 °C maximum cell temperature with a 2.4 °C disuniformity), but become worst performing at 720 s (44.0 °C, 7.2 °C disuniformity). At 720 s, 7 horizontal fins instead become best performing (42.5 °C, 2.6 °C disuniformity) as large thermal gradients caused by convection are suppressed. Overall, we show via a Pareto analysis which geometries offer acceptable trade-offs between thermal performance and TMS mass.

1. Introduction

The ongoing innovation of ultra-low-emissions vehicle (ULEV) technology is a result of the rising demand for clean energy and environmental preservation. Since Lithium-Ion Batteries (LIB) provide a large energy storage density and a long operating life compared to other energy storage technologies, they have been extensively researched as the primary power source for electric vehicles (EVs) [1,2]. Most LIB have a critical temperature of 50 °C. When this temperature is exceeded, the electrochemical process involved in charging and discharging produces a significant amount of heat, which accumulates within the battery pack causing thermal runaway and fire. Additionally, during this event toxic gases are released, causing harm to the environment and living creatures. LIB cells thermal runaway or fire is frequently brought on by harsh circumstances, like high-speed charging/discharging and vehicle accidents. A battery Thermal Management System (TMS) is therefore, required to manage the temperature of LIB cells. TMS can be broadly divided into two categories: active and passive. Active TMS uses fluid like air or liquid (e.g. water, dielectric oil) [3], while passive TMS, e.g. heat pipes and phase change materials (PCM), do not require any active component (fan, pump) to thermally maintain the LIB pack at the desired temperature range [4,5].

PCM-based TMS has numerous benefits over the active system. For instance, they offer uniform cell temperature distribution, low cost, a compact structure, and no parasitic energy consumption [6,7]. However, the PCMs have low heat conductivity, which degrades the TMS's performance [8,9]. Adding fins to the TMS can enhance its thermal performance and speed up the melting of PCM [10–12].

Daneh-Dezfuli and Pordanjani [13] investigated the effect of the number of PCM-filled rectangular cavities (from one to fifteen) on the thermal performance of LIB. It was found that increasing the number of

* Corresponding author.
E-mail address: s.landini@uea.ac.uk (S. Landini).

https://doi.org/10.1016/j.applthermaleng.2024.125216
Received 2 July 2024; Received in revised form 5 December 2024; Accepted 9 December 2024
Available online 15 December 2024

Nomenclature

LIB	Lithium-ion battery
PCM	Phase change material
EVs	Electric vehicles
TMS	Thermal Management System
ULEV	Ultra-low-emissions vehicle
C	Charging / discharging rate
L1	Temperature probe location 1
L2	Temperature probe location 2
DR	Discharge rate
Exp	Experimental results
Num	Numerical results
ρ	Density (kg/m^3)
g	Gravitational acceleration (m/s^2)
A_{mush}	Mushy zone constant
ξ	Liquid fraction
$\in$	Constant values 0.001
h	Sensible enthalpy (J/g)
ΔH	Latent enthalpy (J/g)
S	Source term
V	Velocity (m/s)
C_p	Specific heat (J/kg·K)
k	Thermal conductivity (W/m·K)
H	Specific enthalpy (J/g)
T	Temperature (°C)
ΔT	Temperature disuniformity (°C)
μ	Dynamic viscosity (Nm/s^2)
t	Time (s)
P	Pressure (Pa)
h_{conv}	Convection heat transfer coefficient (W/m^2 ·K)

Subscripts

ave	Average
x	X- direction
y	Y- direction
z	Z- direction
l	Liquid
s	Solid
tot	Total
ref	reference
max	Maximum
med	median value

cavities reduces the maximum and minimum temperatures of the battery. As a result, a uniform temperature through the battery was achieved. Chen, et al. [14], Fan, et al. [15], and Verma and Rakshit [16] examined the effects of cylindrical, vertical fins with various orientation angles, and longitudinal fins along the vertical cross-section of cell battery on the thermal performance of the LIB. It was found that the existence of fins yields a more uniform temperature distribution using 9 horizontal fins, 4 vertical fins at 45°, and 30-mm longitudinal fins maximize PCM use and reduce maximum temperatures by 26 K, improving battery cooling, respectively. Furthermore, Chen, et al. [17] examined the use of PCM in embedded rectangular finned shells to improve thermal management for LIB. The study revealed a 36.7 % decrease in the maximum temperature difference, a 21 % decrease in the average battery-surface temperature, a 15.3 % increase in electric energy output and a 13.2 % increase in maximum discharge capacity. In addition, Dey, et al. [18] explored metal fin hexagonal PCM designs for LIB. The two designs use aluminium rings with vertical fins and vertical interconnecting fins. Results showed that the peak temperature decreased from 336 K (without hexagonal designs) to 308.9 K (with them), a rise reduction of 75.58 %, and a temperature difference reduction of up to 60 %. Sazvar and Moqtaderi [19] investigated the design of stepped fins for LIB. The ratios of the length of the stepped fins to the width of the stepped fins were 0.66, 1, 1.5, 2.33, 4, and 9. The study revealed that stepped fins with a ratio of 9 performed better than other stepped fin ratios in terms of achieving a more uniform heat transfer, resulting in an improvement of 48 %.

Dagdevir and Ding [20] studied the influence of helical fins on the performance of LIB. The study revealed that increasing the width of the helical fin improves the performance of BTMS. However, increasing the number of fin rounds does not linearly lengthen the operating time. Besides, Hong, et al. [21] explored a thermal management system using various T-shaped fin arrangements. It was found that the T-shaped fin with an angle of 135° between the horizontal fins and the left wall of the cavity has the fastest melting time, with rectangular fins at 12.8 % and T-shaped fins at 12.7 %-25.5 %. Rectangular fins reduce wall temperature by 15.0 °C and T-shaped fins by 18.9 °C, improving temperature uniformity by 1.5 % and 2.2 %. It was found that the best T-shaped fin with an angle of 135° between the horizontal and vertical fins lowered wall temperature by 4.9 °C, over other configurations.

Also, Zhang, et al. [22] investigated the impact of branch-fins on the thermal management for LIB. A 3.92 K drop in cell temperature, a 14.98 % improvement in heat transfer, a 131.5 % increase in operating time, and a 10.28 % decrease in system weight was obtained because of improved fin coverage and transverse fins. Moreover, Chen, et al. [23] investigated the influence of bionic spiral fin wrapped with PCM for LIB. It was found that the optimum spiral parameters (winding turns, distance between fin and cold plate, fin thickness, and fin height) that yielded the best results were 15, 0.5 mm, 1 mm, and 1 mm, resulting in a reduction of the maximum temperature by 2.4 °C. Choudhari, et al. [24] and Verma, et al. [25] investigated the thermal performance of the LIB pack using PCM and vertical fins. It was found that insertion fins and using PCM effectively dissipate heat and provide a uniform temperature at the inner cells of the battery pack. Moreover, the maximum temperature reduces by 29.30 K when increasing the thickness of PCM. While, Ahmad, et al. [26] investigated a hybrid system for LIB thermal control combining air and PCM with fins. The study examined the impact of inlet air flow, temperature, thickness of the PCM, diameter, and number of fins. Results reveal that the new hybrid BTMS reduces maximum battery temperature by 18.6 % and 3.2 %, respectively, compared to fin-air and PCM-air BTMS without fins.

In addition, Alghassab [27] conducted an investigation into the cooling performance of circular aluminium and copper fins for LIB. It was discovered that copper fins surpass aluminium fins because copper has a 60 % higher heat conductivity. Suresh and Saha [28] investigated the impact of circular −fin, full-foam fins, and porous fins, on thermal energy storage systems. It was found that the full-foam system melts and solidifies fastest, then solid-fin, porous-fin, and no-fin in order. Full-foam enhances melting temperature performance by 169.9 %, solid-fin 44.8 %, and porous-fin 41.88 %. Porous-fin and full-foam distribute temperature more uniformly than solid-fin and without-fins.

Kim, et al. [29] studied the effects of positing of horizontal fins on LIB performance. It was found that, different horizontal fin arrangements affected heat transfer. For instance, the heat transfer was symmetrical with horizontal fins. The PCM melted faster when fins were placed in the heat sink's vertical centre to evenly transfer heat.

Patel and Rathod [30] investigated the performance of LIB using six commercial organic PCMs. It was found that the RT-42 and RT-50 were suitable to keep the temperature of the battery under 60 °C for all operating conditions. On the other hand, Bais, et al. [31] investigated the effects of using RT-42 for thicknesses of 1 mm to 7 mm. It was found

that the thickness of 4 mm was the most effective thickness to regulate the temperature of the LIB cell. For instance, the thicknesses between 1–3 mm were not enough to absorb the generated heat while the thickness between 5–7 mm act as insulator material when the PCM melted. Also, El Idi, et al. [32] investigated the effects of PCM-Metal Foam composite on the thermal management of LIB. The results revealed that the addition of metal foam to PCM has a great influence on the thermal management of LIB compared to pure PCM. Moreover, Akula and Balaji [33] used PCM along with expanded graphite and pin-fins to enhance the thermal performance of the LIB. Percentages of 10 wt %, 20 wt%, 25 wt%, and 30 wt% of expanded graphite and 130 and 260 fins were used during the investigation. It was found that using 30 wt% of expanded graphite and 260 fins had the great influence on the temperature distribution and reduced the maximum temperature of the battery. Implemented 30 wt% of expanded graphite along with 130 fins was preferred over 260 due to fabrication process. Furthermore, Moaveni, et al. [34] examined a thermal system for LIB using nanoparticles and rectangular-fins. It was found that, adding nanoparticles at 3 % volume fraction lowers battery pack maximum temperature by 0.71 K at 3C discharge rate and 1.28 K at 4C discharge rate. It is also, found that, four fins lower peak temperatures by 4.16 K at 3C and 6.05 K at 4C, while two fins lower them by 5.77 K and 9.87 K, indicating fins work better at higher discharge rates.

Zare, et al. [35] investigated vertical internal-external fins creating PCM silos around the battery surface and discovered that four fins lowered surface temperature by 17.45 K at 5C and 9.90 K at 3C discharge rates compared to systems without fins. This design enhanced the energy density by 10.02 % and the heat storage capacity by 11.11 %, while also ensuring that battery safety was maintained at or below 318.15 K. Wu, et al. [36] studied how PCM-based spaceship BTMS performed when subjected to varying degrees of rotation (0°, 45°, 90°) and accelerations of gravity (0.05g-20g). The PCM melting time reduced by 15 % when the gravity rose to 20g at $\theta = 90°$. A formation of solid PCM was hindered by adjusting the system to $\theta = 45°$, which also caused the system to tilt. Using entropy-weighted TOPSIS, the optimal configuration for PCM melting was found to be a mix of annular and straight fins at $\theta = 45°$. Li, et al. [37] presented a LIB system using 3-D finned tubes and PCM to keep battery temperatures below 45 °C and 2.4 °C. The optimal heat transfer was obtained by optimizing the fin width and axial spacing to balance performance, keeping a PCM liquid–solid ratio above 2:2, as well as fin heights of 4 mm. Akula, et al. [38] incorporated pin fins inside PCM-based heat sinks to improve thermal management of 1LIB. At 5C discharge rate, pin fins reduced battery surface temperature by 3.3 °C more than plate fins. A heat sink with 260 pin fins (1 mm side) optimum performance across heat loads, ambient temperatures, and PCM types.

Furthermore, Najafi Khaboshan, et al. [39] used circular-fins, copper metal foam, and PCM to optimize cooling during 3C discharge in BTMS. The configuration included all techniques, lowered battery temperature by 3 K compared to pure PCM and reduced temperature disparities by 75 % and 66 % under normal and hard circumstances. An artificial neural network model, with R^2 values of 0.98 for PCM liquid percentage and 0.99 for battery temperature, accurately predicted performance, simplifying analysis and providing novel BTMS design insights. Also, Gungor and Lorente [40] proposed a LIB thermal management system using PCM, metallic fins, and liquid cooling. PCM solidifies in between cycles using coolant channels within fins, and it absorbs heat during discharge and charge. This system minimized 2C discharge–charge cycle energy consumption by 54.9 % (from 0.4406 kJ to 0.1963 kJ) compared to liquid cooling. Horizontal fins enhanced PCM melting efficiency, taking ~ 13 min for re-solidification. A summary of the literature review was tabulated in Table 1.

Numerous studies have examined various fin forms and configurations to enhance the thermal management of lithium-ion batteries in phase-change materials. Traditional designs include rectangular and cylindrical fins, as well as more complicated geometries, including triangular and hexagonal. While these designs have the potential to increase heat transfer and temperature uniformity, However, the relationship between fin geometry with system scale and timescale for cell discharge has not yet been thoroughly understood.

The purpose of this study is therefore to examine how fin geometry (shape, angle, and number) impacts the maximum cell temperature and cell temperature disuniformity under both thermal loading and thermal resting conditions. In order to examine the effect of system scale, two differently scaled TMS, are used: a small-scale system with dimensions of the order 10 mm, and a large-scale system with dimensions of the order 100 mm. The thermal properties are examined dynamically, in order to understand how the performance of each fin geometry depend on thermal loading/resting duration.

2. Methodology

2.1. Physical model

A 3D Computational Fluid Dynamics model was developed using ANSYS/Fluent 2022, to investigate the LIB TMS during thermal loading and resting at various discharge rates (DR = 3C,5C).[1] The geometry is illustrated in Error! Reference source not found.(a), which matches the experimental setup of Landini *et al.* [48]. Throughout, this is referred to as the 'small system'. A 'large system' is also employed, being simply a 10-times scale up of the 'small system'. The system features two LIB cells (dark grey), sandwiching a PCM core (orange). All interfaces and external surfaces of this setup are cased in aluminium, except for the top which is open to the ambient atmosphere. The thermophysical properties of the PCM (paraffin wax, commercial 99 %-pure octadecane) and aluminium frame are given in Table 2. In the validation. the LIB cells (AKKU300 pouch cells with mass 7.02 g) are also modelled as aluminium as experiments indicated that the thermal properties of the system were dominated by the aluminium frame and PCM, not the cell material [48]. Aluminium is also used as the model cell material throughout this work to model an ideal benchmark case, not subject to the large variation in thermal properties experienced between cells of different make, age, and batch.

To investigate the thermal profiles of the system under cell discharging (i.e. thermal loading), a uniform volumetric heat generation rate of 122.589 kW/m^3 and 204.311 kW/m^3 for DR = 3C and 5C was applied respectively. These values were obtained experimentally as reported in Landini et al. [48]. To investigate the thermal profiles following the cessation of thermal loading, (i.e. thermal resting), the system is initialised at a uniform temperature of T_l = 30.5 °C, and allowed to cool passively.

2.2. Governing equations

Transient simulations were performed, in which the governing equations of the numerical model used in this study [49,50], can be summarized as follows:

Mass conservation equation, [49,50]:

$$\frac{\partial \rho}{\partial t} + \nabla.(\rho V) = 0 \tag{1}$$

Momentum equation, [49,50]:

$$\frac{\partial (\rho V)}{\partial t} + \nabla \bullet (\rho V) = -\nabla P + \mu \nabla^2 V + \rho g + S \tag{2}$$

[1] LIB are typically tested at constant charge or discharge currents, whose values are reported by using the parameters Charge and Discharge Rate (CR, DR). These are defined as the constant current which charges or discharges the entire nominal capacity of the battery in one hour (e.g. capacity 20Ah, CR=DR=1C, current 20A).

Table 1
Summary of the literature review.

Author	Year	Parameter	Investigation	Charge/ discharge rates (C)	System analysed	Outcomes
Chen, et al. [17]	2024	Cavities using vertical fins	Experimental and numerical	2C	Finned shells configurations	▪ Reductions of 21 % in average battery-surface temperature and 36.7 % in maximum temperature difference were achieved. ▪ PCM solidification improved low-temperature performance by delaying the decline of battery temperature.
Dey, et al. [18]	2024	Fin design	Numerical	4C, 6C, 8C	Fins network	▪ Aluminum rings and vertical fins outperforms aluminum rings and vertical interconnecting fins. ▪ The use of aluminum rings and vertical fins exhibits exceptional thermal management capabilities with respect to both temperature uniformity and peak temperature.
Dagdevir and Ding [20]	2024	Fin shape	Numerical	1C, 2C, 3C and 4C	Helical fin	▪ Helical fins improve heat dissipation by conducting heat in the PCM's low thermal conductivity area.
Chen, et al. [23]	2024	Bionic spiral fin wrapped	Experimental and numerical	3C and 4C	The distance and number of windings turns, height, and thickness,	▪ Optimal spiral fin parameters (thickness 1 mm, height 1 mm, distance to cold plate 0.5 mm, 15 turns) lower maximum temperature by 2.4 °C against no fins. ▪ Spiral fins raise preheating by 5.6 °C. Adjusting winglet number reduces weight by 18 % while maintaining preheating.
Alghassab [27]	2024	Fin material	Numerical	0.5C, 1C, and 1.7C	Aluminum and copper	▪ A reduction in peak temperature of 8 °C can be achieved with 0.2 mm thick and 11.67 mm high fins using 6 copper fins. ▪ A cooling of over 10 °C occurred as the fin height increased from 2 mm to 11.67 mm. ▪ A cooling by over 5 °C occurred as a 4-fin longitudinal setup with a 10 mm height.
Moaveni, et al. [34]	2024	Fins, nanocomposite	Numerical	3C and 4C	2, 4 fin and 3 %-9%	▪ The highest battery temperature drops by 0.71 K at 3C and 1.28 K at 4C discharge rates when 3 % volume fraction nanoparticles are added. ▪ When using four fins instead of none, the battery's peak temperatures drop by 4.16 K at 3C and 6.05 K at 4C.
Zare, et al. [35]	2024	Fin design	Numerical	3C and 5C	Internal and external fins	▪ Battery surface temperature dropped 17.45 K (5C) and 9.90 K (3C) discharge rates with four fins. ▪ Safe operation by keeping surface temperature under 318.15 K.
Wu, et al. [36]	2024	Orientation	Numerical	5C	Gravity and inclination angles	▪ melting time was shortened by 15 % by raising gravity to 20g at $\theta = 90°$. ▪ System tilting to $\theta = 45°$ reduced solid PCM formation but induced tilting.
Li, et al. [37]	2024	Fin design	Experimental	18 W, 36 W and 54 W	3-D finned tube	▪ System battery temperatures were below 45 °C and 2.4 °C different. ▪ Heat transfer was improved using 4 mm fins.
Akula, et al. [38]	2024	Pin fins	Numerical	3C, 4C and C	1.4 mm, 2 mm, 3 mm, 3.5 mm and 4 mm	▪ At 5C discharge rate, pin fins lower temperature by 3.3 °C more than plate fins. ▪ 260 pin fins (1 mm side) perform effectively in all situations.
Najafi Khaboshan, et al. [39]	2024	Fins and metal foam	Numerical	3C	Fins height and fins length	▪ PCM, copper foam, and circular fins lowered battery temperature by 3 K. ▪ Thermal management improved by 75 % under normal and 66 % under extreme conditions.
Gungor and Lorente [40]	2024	design	Numerical	2C	Fins' height	▪ 2C cycle consumption of energy dropped 54.9 % (from 0.4406 kJ to 0.1963 kJ) compared to liquid cooling.
Sazvar and Moqtaderi [19]	2023	Stepped fins	Numerical	Constant temperature of 1 °C	Length / Width	▪ Raising stepped fin length-to-width ratio distributes enclosure heat more uniformly. ▪ A more uniform temperature distribution improves PCM cooling. ▪ Cooling mean power energy is optimized with a length-to-width ratio of 9 and $\phi = 0.1$.
Hong, et al. [21]	2023	T-shaped fin	Numerical	1000 W/m^2	Various arrangements	▪ Rectangular fins shorten the melting time by 12.8 % and T-shaped fins by 12.7 % to 25.5 % when compared to the heat sink without fins. ▪ Rectangular fins cool walls by 15.0 °C. ▪ Wall temperature drops 18.9 °C with T-shaped fins.

(*continued on next page*)

Table 1 (*continued*)

Author	Year	Parameter	Investigation	Charge/ discharge rates (C)	System analysed	Outcomes
						■ Rectangular fins increase temperature uniformity 1.5 %. ■ T-shaped fins increase temperature uniformity 2.2 %.
Zhang, et al. [22]	2023	Vertical branch-fins	Numerical	5C	Various arrangements	■ Increased fin coverage and transverse fins decreased the average cell temperature by 3.14 K and 3.92 K, respectively. ■ Fin coverage angle and lateral fins improved heat dissipation, lowering battery temperature.
Ahmad, et al. [26]	2023	Cylindrical fins	Numerical	5C, 7C and 9C	Fins' number and diameter	■ A PCM thickness of 1.0 mm, 162 fins, and a fin diameter of 3.0 mm characterise the ideal design. ■ Battery temperature can be decreased through improved thermal conductivity and air convection cooling as the number and diameter of fins increase. ■ BTMS uses less fan power with 162 fins, 12 mm pitch, and 3 mm diameter to maintain battery temperatures low.
Suresh and Saha [28]	2023	Fin type	Experimental and numerical	Constant temperature of 69 °C	Porous fin full-foam fin solid-fi	■ Full-foam melts and solidifies fastest, followed by solid-fin, porous-fin, and no fins. ■ Full-foam, solid-fin, and porous-fin have 169.9 %, 44.8 %, and 41.88 % higher temperature response rates than no fins. ■ The liquid fraction is slightly affected by foam porosity than pore density. ■ Porous-fin and full-foam distribute PCM temperature more uniformly during melting and solidification than solid fin and no fins.
Kim, et al. [29]	2023	Horizontal fins	Numerical	10,986.3 W/m^2	Positioning of horizontal fins	■ Centered horizontal fins had the longest SPT and highest storage ratio. ■ Energy storage increased 3.8 % with horizontal fins. ■ Fin arrangements affected energy storage by 2.7 %, suggesting thermal storage optimization.
Daneh-Dezfuli and Pordanjani [13]	2022	Rectangular cavities	Numerical	1C, 1.5C and 2C	Increasing number of cavities 1–15	■ More PCM packs reduced TE-Max and increased the melted PCM volume, leading to faster complete melting. ■ More PCM packs lowered TE-Min initially but increased it over longer periods, with higher charge/discharge rates shortening melting time. ■ TE-Min and TE-Max rose with longer operation times, with melted PCM volume increasing until fully melted. ■ TE-Max did not exceed 325 K under the proposed TLMT system, even in the worst-case scenario.
Chen, et al. [14]	2022	Horizontal fins	Numerical	0.5C, 1C and 1.7C	Increasing number of fins 5–15	■ Increasing the number of fins enhances cooling performance up to nine fins. ■ The maximum battery temperature decreases with up to nine fins. ■ Beyond nine fins, the maximum temperature either remains constant or increases. ■ Optimal fin number for cooling: nine.
Verma and Rakshit [16]	2022	Vertical fins	Numerical	22800 W/m^3-200000 W/m^3	Increasing the fins length 14–30 mm	■ The maximum temperature dropped using 30 mm long longitudinal fins by 26 K, 22 K, and 16 K, for PCM thicknesses of 12 mm, 9 mm, and 7 mm. ■ Thicker PCM layers caused temperature uniformity issues, cooling inner cells more than outer cells. ■ Fins reduced the maximum temperature, requiring less PCM compared to no fins. ■ Increasing PCM thickness absorbed more heat, with 12 mm PCM absorbing the most.
Verma, et al. [25]	2022	PCM thickness, fin length	Numerical	4 W, 11.2 W and 35 W	PCM thicknesses 7 mm-12 mm Fins lengths of 14 mm-30 mm	■ Thick PCM layers lower maximum temperatures but create thermal gradients among cells. ■ Underestimating PCM material can lead to extreme cell temperatures. Optimal thermal performance is achieved with a design range (DR) of 13,007–13,036.

(*continued on next page*)

Table 1 (*continued*)

Author	Year	Parameter	Investigation	Charge/ discharge rates (C)	System analysed	Outcomes
Khan, et al. [41]	2022	Different shapes of PCM chamber	Numerical	1C and 4C	Circular, rhombus, rhombus, square, and hexagonal	▪ The triangular PCM chamber had the lowest TAVE − B and TOU, while hexagonal, and circular cavities had the maximum. ▪ The triangular chamber had the highest HTC, and the lozenge chamber had the lowest. ▪ Early on, the triangular cavity had the greatest PCM melting, and the hexagonal cavity had the minimum. At longer times, the triangular cavity had the greatest, and the lozenge the minimum.
Bais, et al. [42]	2022	Different thicknesses of PCM	Numerical	3C	1 mm to 7 mm	▪ A 4 mm thickness of RT 42 paraffin is optimal for BTMS, with a maximum battery temperature of 42.92 °C at a 3C discharge rate, and PCM remained partially liquefied after 1200 s. ▪ Adding Al2O3/RT 42 paraffin increases the liquid fraction with higher weight fractions. ▪ Increasing Al2O3 nanoparticle weight fraction raises the maximum battery temperature due to reduced latent heat, with the highest temperatures recorded at 42.88 °C for 5 wt% and 42.77 °C for 0.5 wt%.
Amalesh and Lakshmi Narasimhan [43]	2022	Thermal conductivity of PCM flow rates of Dielectric liquid	Numerical	8C	0.2 and 1 W/m K Flow rate 0.5 and 1 lpm	▪ Maintain battery temperature below 40 °C, A 2 lpm coolant flow is required for 8C fast charging. ▪ If the thermal conductivity of PCM is not raised to 1 W/mK or greater, then PCM-based hybrid cooling will not be able to achieve fast charging.
Xin, et al. [44]	2022	Composite PCM and liquid cooling	Numerical	5C	Thickness of 2—8 mm, Expanded graphite percentage between 3—30 %.	▪ CPCM improves heat transfer, reducing temperature and differences in the battery module, with optimal thickness at 4 mm. However, CPCM alone is inadequate for rapid discharge and high temperatures. A hybrid BTMS with CPCM and liquid cooling effectively meets thermal management needs. ▪ At 40 °C ambient and 0.01 m/s coolant velocity, battery temperature decreases with EG up to 12 %, then increases with higher EG. CPCM with 12 % EG provides the best cooling performance, maintaining temperature differences within 5 °C.
Zhu, et al. [45]	2022	Composite PCM and liquid cooling	Experimental and numerical	2C and 4C	Mass fraction 15 %-35 %	▪ The cross-channel arrangement with counter-flow outperforms traditional designs, reducing temperature difference and maximum temperature by 2.5 K, and 4.19 K, respectively, and improving solidification rate by 60.8 %. ▪ Cooling channel cross-section partitions affect solidification rate and CPCM utilization. More partitions enhance CPCM utilization but reduce solidification rate, while fewer partitions lead to poor temperature uniformity and higher battery temperatures. ▪ Increasing EG mass fraction slightly improves CPCM solidification rate but raises maximum temperature and temperature difference. Higher bulk density decreases both solidification rate and maximum temperature.
Fan, et al. [15]	2021	Vertical fins	Experimental and numerical	10 W, 12.5 W and 15 W	Changing the layout of the fins. Length of fins	▪ Optimal 4 fins distribution improved working time by 15.2 %. ▪ Lengthening fins from 7.5 to 13.5 mm increased working time by 8.3 %.
Choudhari, et al. [24]	2021	Fin structure layout	Numerical	1C, 2C and 3C	Vertical fins	▪ The Type III fin structure layout effectively dissipates heat from the inner cells, maintaining outer cell temperatures and achieving uniform temperature distribution within the battery pack. ▪ Including rest periods of 20-, 40-, and 60-minutes during discharge and charge cycles (1C + 3C + 1C + 3C) reduces the average temperature, and PCM melting fraction by 6.45 °C, 7.09 °C, and 7.73 °C, as well as by 0.5 %, 20.9 %, and 40.8 %.

(*continued on next page*)

Table 1 (*continued*)

Author	Year	Parameter	Investigation	Charge/ discharge rates (C)	System analysed	Outcomes
Mousavi, et al. [46]	2021	PCM and mini-channel cold plates	Numerical	50—800 kW/m^3	Battery orientation	▪ Battery module orientation between cold plates greatly affects BTMS performance, with up to 30 K temperature differences. Optimal orientation (case 3) ensures uniform cell temperature, enhancing efficiency and reducing maintenance costs. ▪ HMCP cooling reduces maximum battery temperatures by 0.06, 1, and 10.35 K.
Mohammed, et al. [47]	2021	PCM configurations	Numerical	28,000 W/m^3	Different design of PCMs distribution using three PCMs	▪ Higher latent heat at the top and lower at the bottom provided optimal temperature control at 600 s. ▪ Higher latent heat at the midsection was best at 3600 s. ▪ Design DII excelled at 600 s, but design DIV was superior at 3600 s for thermal performance and uniformity.

Table 2
Thermophysical properties of the system materials [48].

Material	Phase	Thermal properties	Value
Paraffin wax	solid	ρ(kg/m^3)	814
Paraffin wax	liquid	ρ(kg/m^3)	775
Paraffin wax	solid	k(W/m · K)	0.18
Paraffin wax	liquid	k(W/m · K)	0.149
Paraffin wax	solid	C_p(J/kg · K)	2150
Paraffin wax	liquid	C_p(J/kg · K)	2180
Paraffin wax	solid	Solidus temperature (°C)	26.9
Paraffin wax	liquid	Liquidus temperature (°C)	30.2
Aluminium	solid	ρ(kg/m^3)	2719
Aluminium	solid	k(W/m · K)	202.4
Aluminium	solid	C_p(J/kg · K)	871

Table 3
Boundary conditions for validation model [48].

No.	Boundary Location	Heat Transfer Condition		Physical Motivation
1	Top	Convection heat transfer	$q = h_{conv}(T_{surface} - T_\infty)$, where $h_{conv} = 25$ W/(m^2 ·K), $T_\infty = 20.8$ °C	Represents natural convection with ambient air.
2	Bottom	Adiabatic	Solid $\frac{\partial T}{\partial z} = 0$	Model bottom as well-insulated
3	Left	Adiabatic	Solid $\frac{\partial T}{\partial x} = 0$	Model left side as well-insulated
4	Right	Symmetry	Solids and liquid $\frac{\partial T}{\partial x} = 0$	Assume no heat flux through the right side due to symmetry.
5	Front	Symmetry	Solids and liquid $\frac{\partial T}{\partial y} = 0$	Assume no heat flux through front due to symmetry
6	Back	Adiabatic	Solid $\frac{\partial T}{\partial y} = 0$	Model back as well-insulated

Energy equation, [49,50]:

$$\frac{\partial(\rho H)}{\partial t} + \nabla \bullet (\rho V H) = \nabla \bullet (k \nabla T) + S \tag{3}$$

The total enthalpy H_{tot} is combination of the sensible enthalpy h and latent enthalpy ΔH, [49,50]:

$$H_{tot} = h + \Delta H. \tag{4}$$

The sensible enthalpy is evaluated, [49,50] as:

$$h = h_{ref} + \int_{T_{ref}}^{T} C_p dT, \tag{5}$$

where, h_{ref}(245 kJ/kg) is the reference enthalpy at the reference temperature T_{ref} (0 °C). The latent enthalpy, [49,50] is defined as:

$$\Delta H = \xi h_{sl} \tag{6}$$

where, ξ is the PCM liquid fraction and h_{sl} is the latent heat of melting of the PCM.

The liquid fraction, can be evaluated, [49,50] as follows:

$$\xi = \begin{cases} 0 & T < T_s \\ \dfrac{(T - T_s)}{(T_l - T_s)} & T_S < T < T_l \\ 1 & T > T_l \end{cases}, \tag{7}$$

where, T_s and T_l represent the solidus and liquidus temperatures of the PCM, respectively.

The source term, S, is utilized to gradually lower the velocities from a finite value in the liquid phase to zero in the fully solid phase over the computational cells that encounter a phase change, [49,50] and calculated as follows:

$$S = \frac{(1 - \xi)^2}{(\xi^3 + \epsilon)} A_{mush} V, \tag{8}$$

where A_{mush} is the mushy zone constant, which impacts the damping of the fluid velocity into the solid region, and also influences the solution stability [51]. A value of$A_{mush} = 10^4$ is used here, within the 10^4-10^7 range recommended [51]. Larger mushy zone constants were tested, however for $A_{mush} > 10^4$, the simulations became numerically unstable before melting of the PCM had completed. Using$A_{mush} = 10^4$ is further justified through the agreement between numerical and experimental results, shown in the validation (Section 2.5).

2.3. Solution Methodology

Within ANSYS/Fluent 2022, the pressure-based solver and the SIMPLE algorithm was used to solve the governing equations, the least squares cell based was used for spatial discretisation, the PRESTO solver was used to solve the pressure term, and the second order upwind was used to solve the momentum and energy equations. The conversion criteria for the governing equations were set to be 10^{-6} to obtain high

accuracy for the numerical solution. The relaxation factors of 0.3, 1, 1, 0.7, 0.9, and 1 were used for the pressure, density, body force, momentum, liquid fraction, and energy, respectively.

Due to the symmetry of the system, in the numerical model one quarter of the system was simulated, illustrated in Fig. 1(b). This illustration also labels each of the six eternal boundary conditions, which correspond to the descriptions that are described in Error! Reference source not found. for the validation simulations, and Table 4 for the thermal loading resting simulations with differing fin geometries. Throughout, all mass transport boundary conditions of the fluid domain (the PCM-filled region) are no-slip with no advection across the boundaries.

2.4. Mesh and Sensitivity study

The computational domain was discretised into a hexahedral mesh, with the illustration in Error! Reference source not found.(c) showing a typical example. To examine the impact of both space and time discretisation on the simulated outcomes, the small-scale system was initialised at a uniform temperature of 21.6 °C, and then 5C thermal loading conditions were applied. The liquid fraction was tracked as the temperature of the PCM rose and melting occurred. This simulation was repeated for a range of mesh densities and timestep sizes, as shown in Fig. 2. It was found that a domain with 2.94×10^5 cells offered a suitable balance of accuracy and computational time, as did a timestep size of 0.1 s. These system properties are used throughout this work.

2.5. Validation

The numerical results were validated against the experimental setup of Landini et al [48]. In the experiments, the small-scale system was initialised at a uniform ambient temperature of 20.8 °C, and either a 3C or 5C discharge applied to the cells to thermally load the system. To match the experimental system, the boundary conditions in the numerical model are defined in Table 3.

Two temperature sensors were inserted within the PCM bulk at 9 mm (location L1) and 27 mm (location L2) measured from the top surface, as illustrated in Error! Reference source not found.(a). The temperature at these probes was recorded over time at 1 Hz frequency, with the results plotted as the dashed red and black lines for the 5C and 3C discharge rates respectively in Fig. 3. Experimental calibration of the temperature probes suggested a temperature uncertainty of ± 0.22 K. This uncertainty is indicated by the shaded regions surrounding the experimental temperature profiles. Meanwhile, the temperature profiles from the matching simulations are shown as solid lines. In Fig. 3(a), it can be seen that for temperature probe location L1, the experimental results and simulations agree to within the error margins of the temperature uncertainty. This is also observed in Fig. 3(b) for probe location L2 under the 3C discharge, but for the 5C discharge the simulations and experiments deviate slightly up to a maximum of 0.5 K. However, given the other sources of uncertainty present in the experimental system, such as the 8 % uncertainty in heat generation rate, and the unknown deviation of the cell heat generation uniformity, it is reasonable to conclude that the simulations and experiments are in agreement.

2.6. Geometry and boundary conditions

The principal aim of this work is to understand how the type and geometry of aluminium fins, extending into the PCM, impacts both the maximum temperature and temperature homogeneity of the cell. A range of fin geometries were tested, illustrated in Fig. 4. Five main types were tested with design variants of each. Note that in this section, all dimensions are given for the small-scale system; for the large-scale system, all dimensions and thicknesses are scale up by a factor of 10. The systems tested were: the original system with no fins; vertical fins (either 5 fins separated by 3.416 mm, or 9 fins separated by 1.85 mm), horizontal fins (3, 5, and 7 fins separated by 9 mm, 5.83 mm, and 4.25 mm respectively), then 'A-shaped' and 'V-shaped' fins (7 fins separated by 4.25 mm, at inclination angles of 10°, 15°, and 20°). Anticipating the results, the A-shaped and V-shaped fins were designed as variations on the best-performing system (horizontal, 7 fins) to examine the impact of only semi-partitioning the PCM, and the effects of buoyancy. The thickness of each fin was 0.5 mm.

The aim with the vertical and horizontal fins was to explore how partitioning the PCM into either vertical or horizontal regions would impact the cell temperature profile. With the A-shaped and V-shaped fins, the aim was to partition the system only partially, and explore the impact of buoyancy. The boundary conditions during the thermal load and thermal resting are listed in Table 4.

3. Results

3.1. Thermal loading

3.1.1. Small-scale system

To begin with, the small-scale systems are examined under the thermal loading conditions corresponding to a 5C cell discharge, with the results summarised in Fig. 5. In Fig. 5(a), (b), and (c), the maximum battery temperature T_{max}, maximum temperature difference ΔT, and PCM liquid fraction are plotted against time respectively. For visual clarity, out of each type of fin design tested, only temperature profiles from a representative sample are shown. Note that in experiments, a 5C

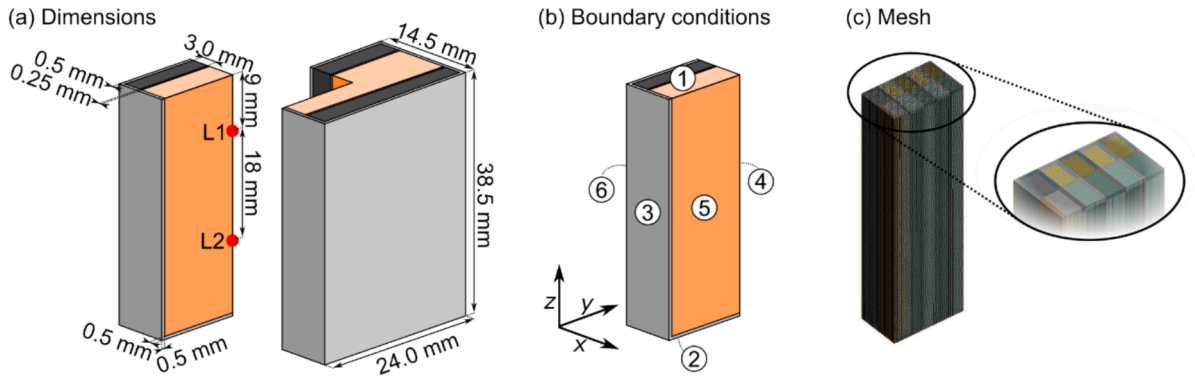

Fig. 1. (a) The geometry of the small-scale system used in [48], with cut-out showing the internal geometry. The large-scale system also considered is 10 times scale-up of this. L1 and L2 indicate the locations of the temperature sensors used in experiments and compared to for numerical validation. (b) Illustration of the simulation domain, one quarter of the whole system, with numbers labelling the external boundary conditions that are tabulated in Error! Reference source not found. and Table 4. (c) Discretisation of the computational domain into a hexahedral mesh.

Table 4
The boundary condition during the numerical investigation.

No.	Boundary Location	Heat Transfer Condition		Physical Motivation
Thermal loading				
1	Top	Adiabatic	Solid and liquid $\frac{\partial T}{\partial z} = 0$	No heat flux across the surface for both fluid and solid.
2	Bottom	Adiabatic	Solid $\frac{\partial T}{\partial z} = 0$	No heat flux across the surface for both fluid and solid.
3	Left	Adiabatic	Solid $\frac{\partial T}{\partial x} = 0$	No heat flux across the surface for both fluid and solid.
4	Right	Symmetry	Solid and liquid $\frac{\partial T}{\partial x} = 0$	Assumes no heat flux through the boundary due to symmetry.
5	Front	Symmetry	Solid and liquid $\frac{\partial T}{\partial y} = 0$	Assumes no heat flux through the boundary due to symmetry.
6	Back	Adiabatic	Solid $\frac{\partial T}{\partial y} = 0$	No heat flux across the surface for both fluid and solid.
Thermal resting				
1	Top	Convection heat transfer	$q = h_{conv}(T_{surface} - T_{\infty})$, where $h_{conv} = 5$ W/(m^2·K), $T_{\infty} = 15$ °C	Represents natural convection with ambient air.
2	Bottom	Convection heat transfer	$q = h_{conv}(T_{surface} - T_{\infty})$, where $h_{conv} = 5$ W/(m^2·K), $T_{\infty} = 15$ °C	Represents natural convection with ambient air.
3	Left	Convection heat transfer	$q = h_{conv}(T_{surface} - T_{\infty})$, where $h_{conv} = 5$ W/(m^2·K), $T_{\infty} = 15$ °C	Represents natural convection with ambient air.
4	Right	Symmetry	Solid and liquid $\frac{\partial T}{\partial x} = 0$	Assumes no heat flux through the boundary due to symmetry.
5	Front	Symmetry	Solid and liquid $\frac{\partial T}{\partial y} = 0$	Assumes no heat flux through the boundary due to symmetry.
6	Back	Convection heat transfer	$q = h_{conv}(T_{surface} - T_{\infty})$, where $h_{conv} = 5$ W/(m^2·K), $T_{\infty} = 15$ °C	Represents natural convection with ambient air.

discharge, by definition, lasts 720 s (indicated by the dotted vertical line). However, in simulations, the heat generation rate can be applied for longer to examine longer timescale changes under these high thermal loading conditions.

In Fig. 5(a), for all systems it can be seen that for the first 70 s of thermal loading, heat is transferred sensibly to the solid PCM and the temperature of the whole system increases. At 70 s, Fig. 5(c), shows the PCM begins to melt, so that up to 720 s, the majority of heat evolved from the cell is absorbed as latent heat in melting the PCM. By 900–1000 s, all systems show a full melting of PCM, at which point the cell temperature rises quickly as heat is transferred sensibly to the liquid PCM.

Before detailing the relative thermal performances of each fin geometry, it is instructive to examine Fig. 5(b). It initially may be concluded, for example, that the no-fin system is always outperformed by any of the finned systems, as the temperature is always more inhomogeneous in the no-finned system (ΔT is larger). However, examining the vertical scale shows that the ΔT of all the systems are within at most 0.2 °C of each other. Practically therefore, this small difference is not sufficient to meaningfully distinguish between different fin designs. This is exemplified by the colour maps showing the temperature and PCM liquid fraction at 720 s in Fig. 5(d) and Fig. 5(e) respectively. Here, the temperature variation between systems is small, and the PCM liquid fraction is relatively uniform: there are no clear regions of solid or liquid. This is due to the system scale: although the thermal conductivity of solid PCM is low, the small system scale means that even under 5C discharge conditions, there is sufficient time for a uniform temperature distribution to be maintained across the entire PCM volume. It is concluded then, that fin geometry has no meaningful impact on the cell thermal profile for the small-scale system.

3.1.2. *Large-scale system*

In contrast to the small-scale system, in the large-scale system (a 10 × scale-up), large temperature and PCM liquid fraction inhomogeneities are observed. Fig. 6(a–c) shows how T_{max}, ΔT, and PCM liquid fraction, respectively vary with time under 5C thermal loading. This is shown for the same representative selection of fin geometries as in Fig. 5. To examine the efficacy of the PCM and fin combination, snapshots of the PCM temperature and liquid fraction are shown in Fig. 6(d) and (e) respectively at times $t = 240$ s, 480 s, 720 s, and 960 s.

In the no-fin system across the time range, Fig. 6(d) and (e) show how hot, liquid PCM accumulates at the top of the system, and cold, solid PCM at the bottom. Thus, the cell is exposed to a large PCM temperature gradient, resulting in $\Delta T = 8.6$ °C across the cell at 720 s. Meanwhile, out of all the systems, the no-fin system shows the lowest melting rate in Fig. 6(c). Thus, heat is not effectively transferred to the PCM, resulting in a large cell temperature of $T_{max} = 51.8$ °C at 720 s.

Interestingly, for $t \geq 480$ s, the vertical, 9-fin system also shows similar PCM liquid fraction temperature distributions, resulting in a large $\Delta T = 7.2$ °C at 720 s. However, the large surface area of the fins is sufficient to maintain a relatively low $T_{max} = 44.0$ °C at 720 s. For $t <$ 480 s, the vertical fin geometry is the optimally performing geometry, both in terms of maintaining a low ΔT across the cell and maintaining a low T_{max}.

This occurs because again, the high surface-area of the fins is able to conduct heat into the PCM effectively, but at $t < 480$ s, there has not been sufficient time for liquid PCM to rise and establish a large temperature gradient. For timescales less than the convection timescale, a large surface area fin geometry is optimal.

The thermal profile of the horizontal-fin systems differs markedly. Although in Fig. 6(c) the PCM melting rates are comparable between the vertical and horizontal fin systems, in Fig. 6(e) it can be seen that horizontally partitioning the system means that the liquid and solid PCM is distributed more evenly over the cell surface. The consequence of this, as shown in Fig. 6(d), is that the cell temperature remains much more uniform over the thermal loading duration. At 720 s, $\Delta T = 2.6$ °C, the lowest of all fin geometries tested. In terms of maintaining a low cell temperature however, the vertical fin system is still best-performing up to $t = 620$ s. For $t > 620$ s, the horizontal fins are best-performing. Thus, horizontal fins are a solution if low temperature inhomogeneity is desirable, or the thermal loading is applied for long timescales.

The A-shaped and V-shaped fins feature a semi-open design, in which liquid PCM can explore the full height of the system only close to the

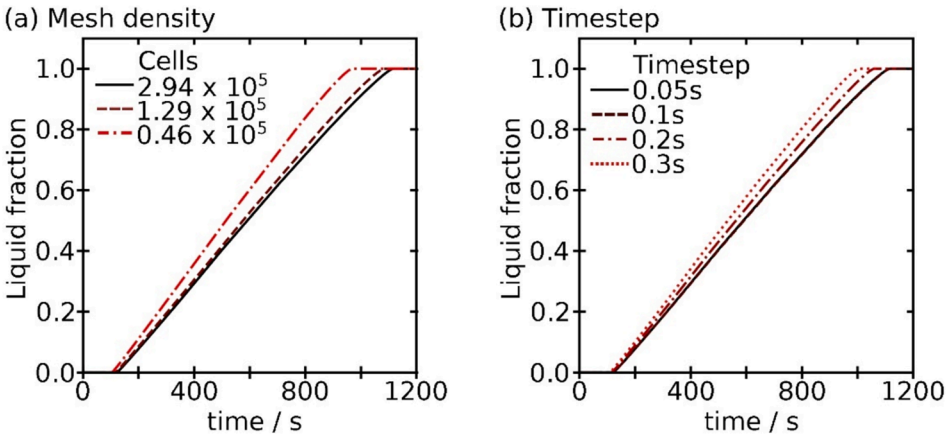

Fig. 2. Sensitivity study conducted for the small system with no fins under 5C thermal loading conditions. The liquid fraction of PCM is tracked over the melting transition for a range of mesh densities (a) and simulation timestep sizes (b).

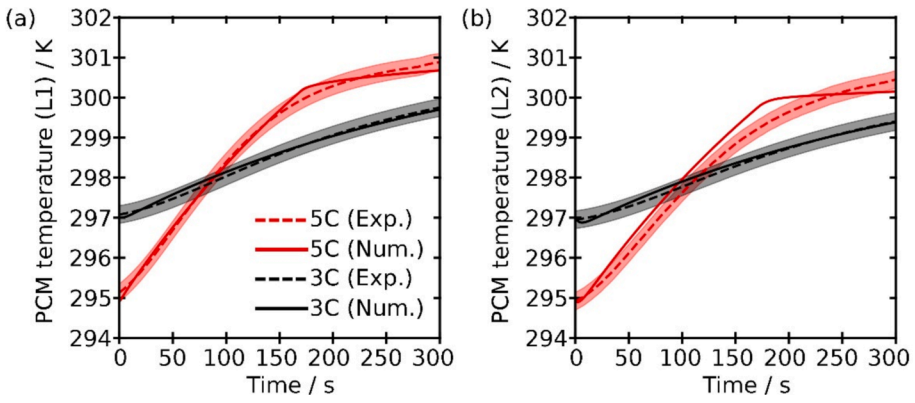

Fig. 3. Validation of the numerical model against experiments. (a) Indication of the two temperature measurement locations L1 and L2. (b, c) Numerical vs. experimental comparison of the time variation of PCM temperature at location L1 (b) and L2 (c) under 3C (black) and 5C (red) thermal loads. Simulation data is indicated via solid lines, experimental data as dashed lines, with shaded regions indicating the range of experimental temperature measurement uncertainty.

domain boundary. For $t > 480$ s therefore (when liquid PCM has had sufficient time to rise), the fins are only partially effective at reducing the temperature gradient placed on the cell. At 720 s, ΔT for the A-shaped and V-shaped fins in Fig. 6(b) is 4.5 °C and 3.7 °C respectively, between that of the vertical and horizontal fins. Fig. 6(c) shows that the PCM in the V-shaped fins melted at a slower rate than for the A-shaped fins. In Fig. 6(e), this can be seen as the V-shaped fins maintaining a larger volume of solid PCM distributed throughout the system than for the A-shaped fins. Thus, the ability of fins to maintain a low ΔT follows from the efficacy of maintaining solid PCM distributed throughout the system volume.

3.2. Thermal resting

3.2.1. Small-scale system

Upon cessation of thermal loading, it is useful to observe how quickly the PCM re-solidifies, and how in doing so, the cell is maintained at an approximately constant temperature. In Fig. 7(a–c) respectively, the evolution of T_{max}, ΔT, and PCM liquid fraction, is shown, starting from an initial system at a uniform temperature of 50 °C (ensuring all PCM is liquid). Heat loss from the system occurs passively via the external boundaries.

In Fig. 7(a), all small-scale systems cool from 50 °C to the liquidus temperature, $T_l = 30.5$ °C in approximately 1.33×10^3 s (22 min). After this, the cooling rate slows dramatically as the PCM solidifies, as shown in Fig. 7(c). There is little difference between the cooling rates between all fin geometries, although it is observed that due to the extra volume of PCM compared to aluminium fin, the no-fin system takes 23 % longer to cool to the solidus temperature $T_s = 28.5$ °C than the vertical 9-fin system. For comparison, the volume of PCM in the no-fin system is 26 % larger than in the vertical 9-fin system.

Due to the long timescale of cooling relative to the thermal conduction rate through the small-scale PCM volume, as is shown in Fig. 7 (d) and (e), the PCM liquid fraction and PCM temperature remain largely uniform throughout the thermal resting process. Thus, as seen in Fig. 7 (b), the ΔT across the cell is of the order of 0.01 °C for all fin geometries. Although small, the observed spike in temperature at the onset of solidification is due to the formation of hot spots in the solidifying liquid. However, relative to the no-fin system, all fined systems are effective at homogenising the temperature distribution arising from inhomogeneous solidification.

3.2.2. Large-scale system

In contrast to thermal loading, for thermal resting the temperature and liquid fraction profiles for the large system are similar to the small system, although with all timescales extended by approximately a factor of 10. In Fig. 8 (a–c) respectively, the evolution of T_{max}, ΔT, and PCM liquid fraction, is shown for the large-scale system. In Fig. 8(a), again, all systems exhibit a relatively quick initial decrease in T_{max} up to $t = 1.36 \times 10^4$ s (3.8 h). Following this, the PCM solidifies as shown in Fig. 8(c), with the ultimate solidification time dependent on the volume of PCM in the system. Unlike for melting, the long cooling timescale means that the PCM liquid fraction and temperature remain largely uniform throughout the system, illustrated in Fig. 8 (d) and (e). This leads to small

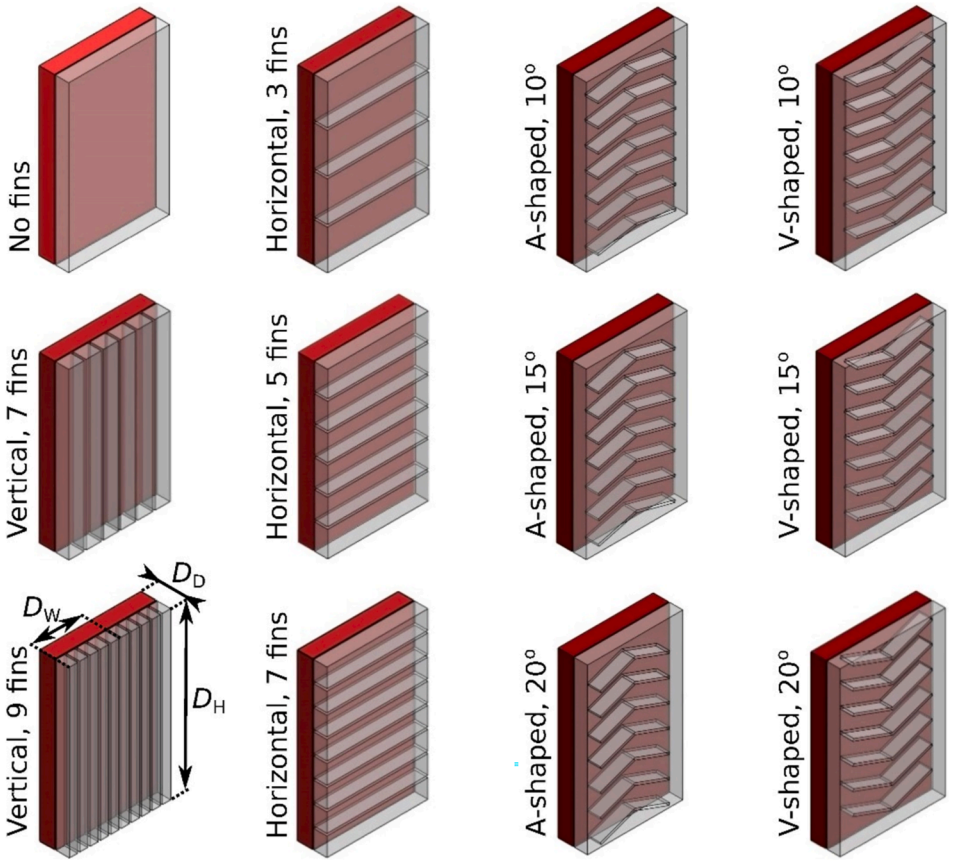

Fig. 4. Illustration of the aluminium fin geometries that extend from the cell (red) into the PCM (translucent grey). Due to symmetry, the computational domain is one half of that shown, with dimensions D_W, D_D, and D_H shown in the bottom, left-hand panel, corresponding to the domain width, depth, and height respectively. For the small scale system, $D_W = 11.5$ mm, $D_D = 6.75$ mm and $D_H = 38$ mm.

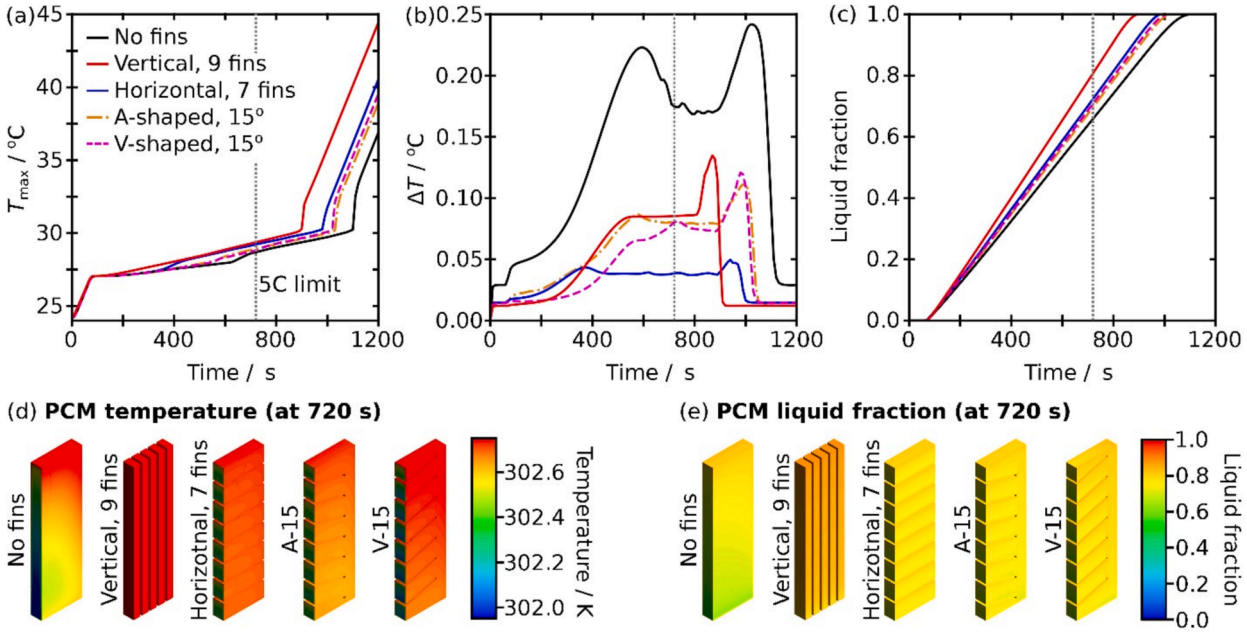

Fig. 5. Evolution of the temperature profile and PCM liquid fraction during thermal loading (5C) of the small system. (a-c) Time evolution of the: maximum temperature in the cell (a), maximum temperature difference across the cell (b), and liquid fraction in the PCM (c), for five representative fin geometries. Due to the small differences in thermal properties of each geometry, a snapshot is shown only at 720 s for the PCM temperature profile (d), and local PCM liquid fraction (e).

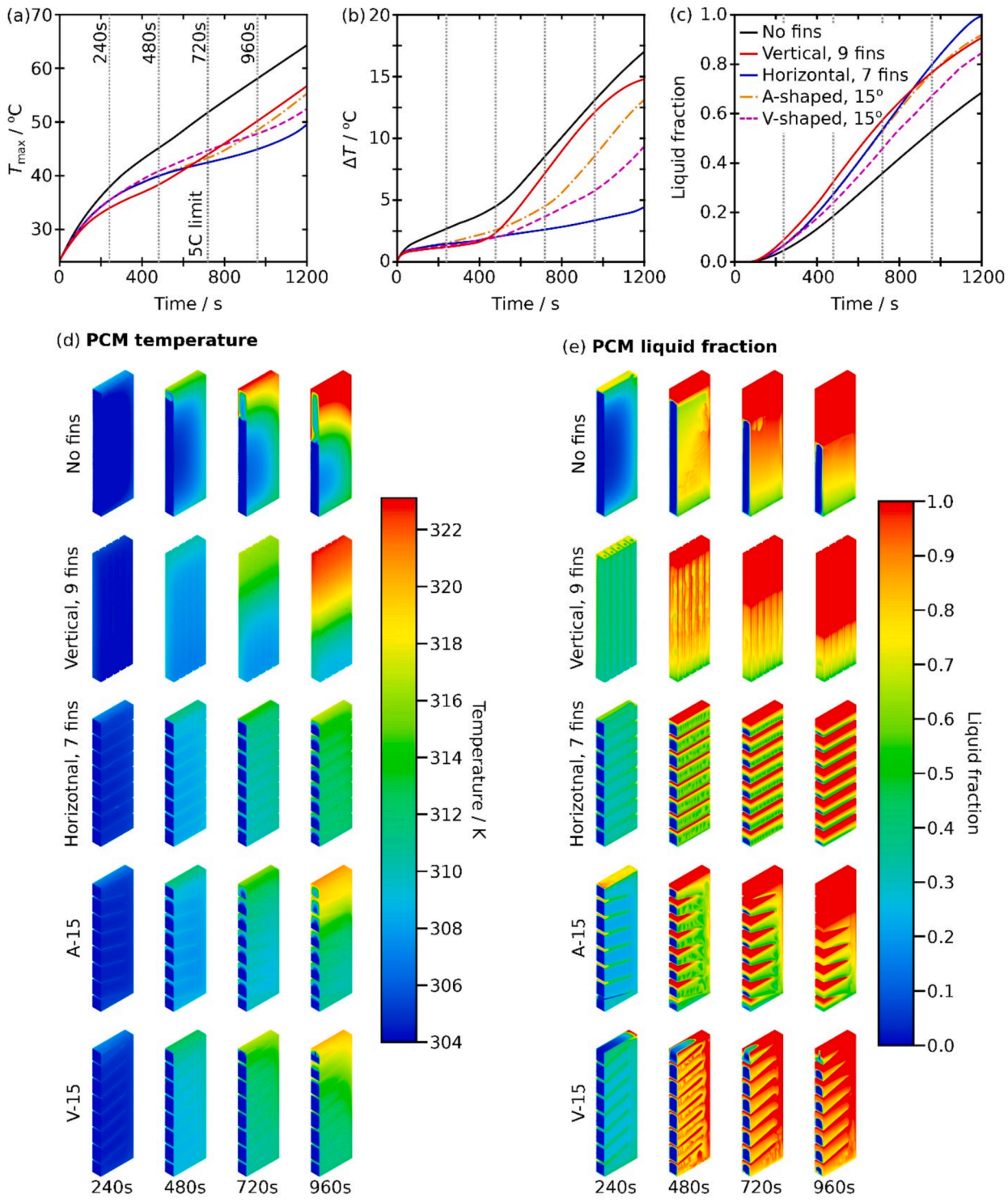

Fig. 6. Evolution of the temperature profile and PCM liquid fraction during thermal loading of the large system. (a-c) Time evolution of the: maximum temperature in the cell (a), maximum temperature difference across the cell (b), and liquid fraction in the PCM (c), for five representative fin geometries. (d) Snapshots of the PCM temperature profiles at 240 s, 480 s, 720 s (the 5C limit) and 960 s. (e) Snapshots of the local liquid fraction in the PCM as time evolves.

temperature differences across the cell in Fig. 8(b), of the order of 0.1 °C.

4. Pareto analysis

Having evaluated the temperature distributions the cell experiences for a variety of fin geometries, in Fig. 9, a Pareto chart method is used to evaluate the best-performing system designs, as performed by Landini, et al. [52] for example. In this, we define two objective functions, a thermal objective function and a mass objective function. The thermal objective function is based on two key metrics that should ideally be minimised for optimal cell performance: the maximum cell temperature T_{max} and the cell temperature inhomogeneity ΔT. As both parameters are time dependent (as shown in Fig. 5 and Fig. 6), a choice exists in how these parameters are entered into the Pareto analysis. Here, we make two choices. The first is to evaluate the maximum value of T_{max} and ΔT that occur for each system during the first 720 s of thermal loading.

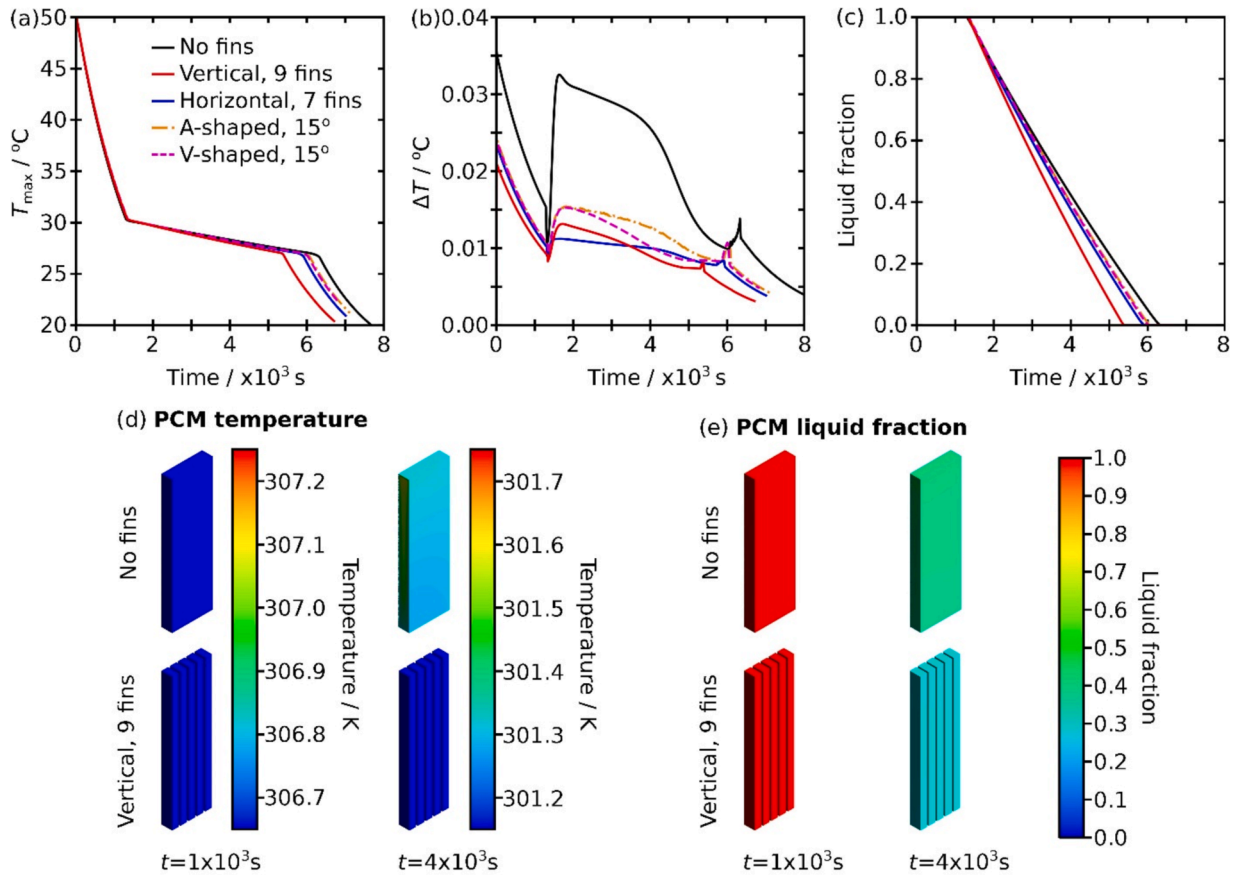

Fig. 7. Evolution of the temperature profile and PCM liquid fraction during the cell rest period of the small system, starting from a fully melted PCM. (a-c) Time evolution of the: maximum temperature in the cell (a), maximum temperature difference across the cell (b), and liquid fraction in the PCM (c), for five representative fin geometries. Due to the small differences in the cooling profiles of each geometry, PCM temperature profiles (d) and local liquid fraction (e) are shown at 1,000 s, and 4,000 s only for the no-fin and 9-vertical fin geometries.

These are labelled T_{max}(max) and ΔT(max) respectively. 0 s – 720 s is chosen as the evaluation interval, as this corresponds to 5C cell discharging conditions as mentioned previously. The thermal objective function is the product T_{max}(max).ΔT(max). For all systems tested, T_{max}(max) and ΔT(max) occurred at 720 s, so this thermal objective function reflects the thermal profile of the cell at the end of the thermal loading period.

The second choice is to average the values of T_{max} and ΔT across the first 720 s of thermal loading. These are labelled T_{max}(med) and ΔT(med), with 'med' indicating that the median was taken. The thermal objective function using these values is the product T_{max}(med).ΔT(med). Systems with a low T_{max}(med).ΔT(med) are characterised as having, on average across the 5C discharge, both low cell temperatures and high temperature uniformity.

For the mass objective function, the percentage increase in mass that the PCM and fins add relative to the system without this TMS, i.e. LIB, is chosen. The mass objective function therefore captures the trade-off when installing such a TMS: cell temperature characteristics are improved, but at the expense of adding weight to the system.

In Fig. 9 (a), the Pareto chart is shown for the large-scale system with the thermal optimisation function T_{max}(max).ΔT(max). From a thermal perspective, all three horizontal fin systems perform well, and are able to minimise both T_{max} and ΔT at the 720 s point, as discussed in the large-scale thermal loading section. The A-shaped and V-shaped fins perform similarly, but the vertical fins show a poor improvement over the no-fin system, due to the large cell temperature and temperature gradients observed at $t = 720$ s.

In Fig. 9 (b), the Pareto chart for the large-scale system with the thermal optimisation function T_{max}(med).ΔT(med) is shown. In contrast to Fig. 9 (a), the vertical fins (particularly the 9-finned system) now show markedly improved thermal properties relative to the no-fin case. It was reasoned in Fig. 6 that for the first 480 s of the 720 s thermal loading, the large fin surface area was able to effectively transfer heat from the cell to the PCM, and maintain a uniform temperature distribution. However, although the vertical 9-fin system has favourable average thermal properties, the quantity of aluminium required for the fins does make this the heaviest system to implement. Interestingly, the V-shaped fins at a 10° inclination show the overall best thermal performance, not the horizontal 7-fin system. This is due to the V-shaped fins having a marginally smaller T_{max} and ΔT across the first 600 s of thermal loading. The horizontal 7-fin system only outcompetes this in the final 120 s of thermal loading. If a low mass is preferable over a high thermal performance, the horizontal 3-fin system offers markedly better thermal properties than the no-fin system, with only a small mass penalty.

In Fig. 9 (c), and (d), Pareto charts for the small-scale system are shown with thermal objective functions T_{max}(max).ΔT(max) and T_{max}(med).ΔT(med) respectively. For the small-scale systems, there is relatively little change in the relative thermal performance between both thermal optimisation functions. In both, the vertical 5-, and 7-fins, and the horizontal 3- and 5-fins perform well thermally, with the horizontal 3-fin system having the lowest mass increase relative to the no-fin system. However, it is important to be mindful of the key conclusion drawn from Fig. 5: the small system scale means that practically speaking, the fins contribute little to the thermal performance relative to the no-fin system.

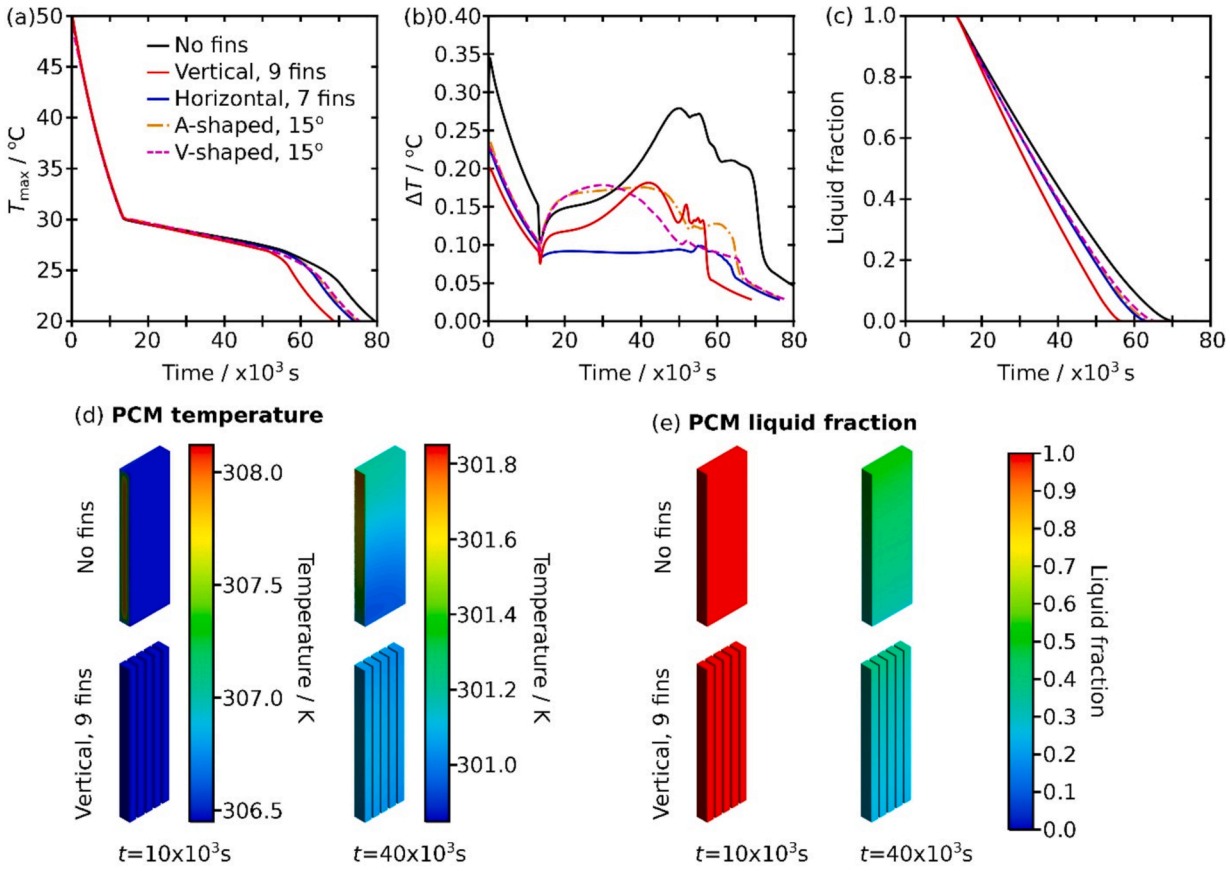

Fig. 8. Evolution of the temperature profile and PCM liquid fraction during the cell rest period of the large system, starting from a fully melted PCM. (a-c) Time evolution of the: maximum temperature in the cell (a), maximum temperature difference across the cell (b), and liquid fraction in the PCM (c), for five representative fin geometries. Due to the small differences in the cooling profiles of each geometry, PCM temperature profiles (d) and local liquid fraction (e) are shown at 10,000 s, and 40,000 s only for the no-fin and 9-vertical fin geometries.

5. Conclusion

In this work, a numerical model was developed in Ansys Fluent to examine the melting and solidification profiles of a Phase Change Material (PCM) – based passive thermal management system (TMS), for the application of cooling and improving temperature uniformity across a lithium-ion cell under 5C discharge conditions. The principal aim of this work was then to explore the efficacy of different aluminium fin geometries at enhancing both the cooling and temperature uniformity properties, and examine how this efficacy changed with both the TMS system scale and thermal loading/resting duration.

To begin with, the numerical model was established and validated against the experimental system of Landini *et al.* [48]. A variety of differing fin geometries were then applied in the model, including horizontal, vertical, and arrow-shaped fins ('A'-shaped and 'V'-shaped). Two different system scales were examined: a small-scale system with dimensions of the order of 10 mm, and a large-scale system with dimensions of the order 100 mm.

For small-scale systems, fins offered no meaningful improvement on the thermal properties compared to PCM alone: at the end of a 720 s discharge, the maximum cell temperature was 29.8 °C for the no-fin system, compared to 29.7 °C with the best-performing A-shaped fins. The maximum temperature difference recorded under loading was only 0.25 °C. This was because, despite the low thermal conductivity of PCM, the small system dimensions (38.5 × 24 × 14.5) mm meant that a relatively uniform temperature could be maintained throughout the entire system during both thermal loading and thermal resting. For such small systems therefore, no fins are required to achieve near-optimal performance.

In contrast, when scaling up each system dimension by a factor of 10, the fin geometry substantially influenced the temperature profiles under thermal loading, but not thermal resting. Interestingly, the efficacy of the fins under loading conditions depended on the timescale that the thermal discharge was applied for. For example, after 480 s of discharge, for the no-fin system, the maximum cell temperature was 45.1 °C with a temperature disuniformity of 4.5 °C, compared to 9, vertical fins: 38.3 °C with a disuniformity of 2.4 °C. At 720 s, the no-fin system showed a maximum cell temperature of 51.8 °C and disuniformity of 8.6 °C. For the 9, vertical fin system, the maximum cell temperature was 44.0 °C with a large, 7.2 °C, disuniformity, as PCM convection causes large thermal gradients, degrading performance. In contrast, 7, horizontal fins maintain a relatively low maximum cell temperature (42.5 °C) and disuniformity (2.6 °C).

Finally, given the survey of fin geometries and temperature profiles, a Pareto-style analysis was used to indicate the best-performing fin geometries. In this analysis, two objectives were considered: (1) a mass objective, with the aim of minimising the weight of the passive thermal management system, (2) a thermal objective, with the aim of minimising both the battery temperature and temperature disuniformity. For the large system, if the desired aim was to reduce the maximum temperature and temperature disuniformity across the cell during the 720 s discharge, 7 horizontal fins showed the best thermal performance, with the fins and PCM increasing the system mass by 20 %. 3 horizontal fins were the lightest (increasing the mass of the system by 18 %), and also showed substantially improved thermal properties over the no-finned system. If instead, the desire was to reduce the average maximum temperature and temperature disuniformity across the 720 s of discharge, then the V-shaped fins at 10° of inclination showed the best

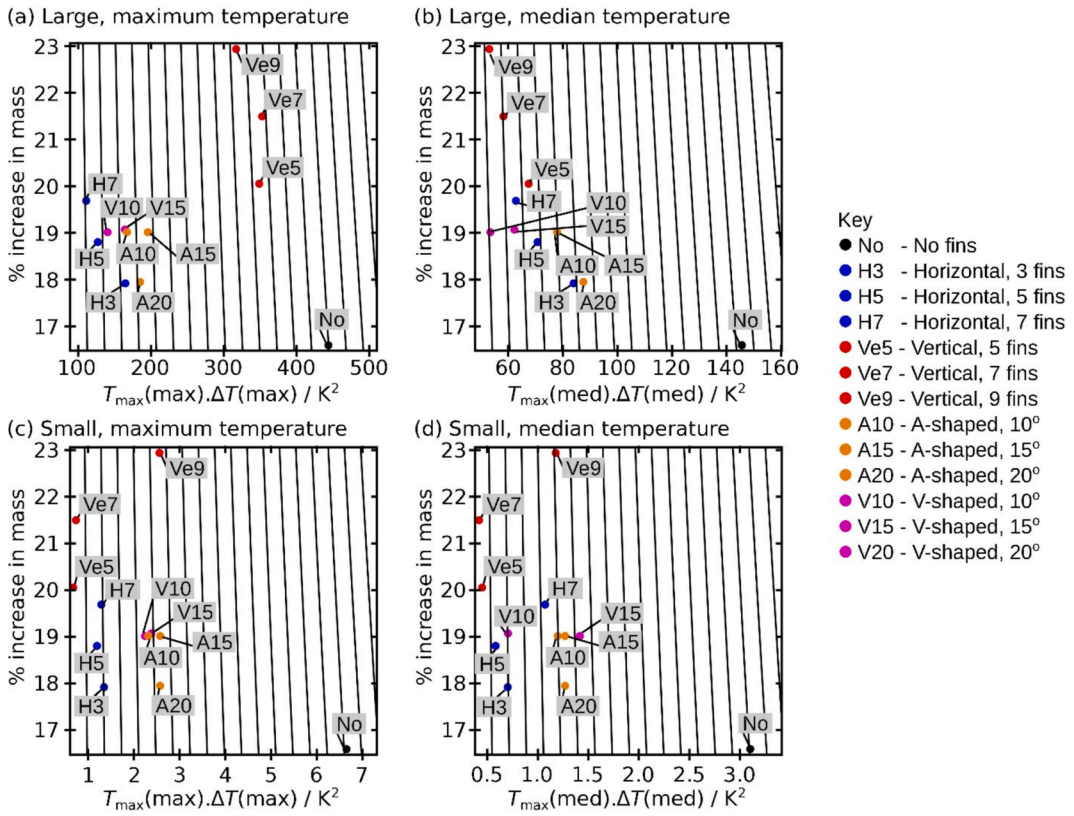

Fig. 9. Pareto charts indicating system designs based upon thermal performance (horizontal axes) and % increase in mass of the system due to inclusion of the PCM and fins. T_{max}(max) and ΔT(max) are the maximum values of T_{max} and ΔT observed respectively during the first 720 s of 5C thermal loading. T_{max}(med) and ΔT(med) are the median values of T_{max} and ΔT observed respectively during the same interval. The contours map the product of the thermal performance and mass performance metrics. (a) Large system with maximum temperature thermal performance. (b) Large system with median temperature thermal performance. (c) Small system with maximum temperature thermal performance. (d) Small system with median temperature thermal performance.

thermal properties, and contributed a 19 % increase in the system mass.

Overall, this study has shown how the scale of the TMS and typical discharge time impacts which fin geometry is best suited to maintaining low cell temperature and low temperature disuniformity. A limitation of this work is that both the cell discharge rate and external conditions were constant in time. Given the clear time-dependent efficacy of different fin geometries, future work will therefore be expanded to include cyclic thermal loading scenarios, changeable climatic conditions, and dynamic discharge rates in order to mimic real-life use cases. Likewise, this work also modelled the cell in an idealized way – providing a spatially uniform heat generation rate. Future work will model the inherent non-uniformity in heat generation rate from real cells. Finally, although a range of fin geometries were examined here, the design space remains broad and largely unexplored. It will be interesting therefore to perform a comprehensive optimization on fin geometry, in order to optimize thermal performance while minimizing such considerations as TMS mass and material cost.

Funding sources

This research did not receive any specific grant from funding agencies in the public, commercial, or not-for-profit sectors.

Declaration of competing interest

The authors declare that they have no known competing financial interests or personal relationships that could have appeared to influence the work reported in this paper.

Data availability

Data will be made available on request.

References

[1] S. Landini, J. Leworthy, T.S. O'Donovan, A review of phase change materials for the thermal management and isothermalisation of lithium-ion cells, J. Energy Storage 25 (2019).
[2] S. Landini, T.S. O'Donovan, Novel experimental approach for the characterisation of Lithium-Ion cells performance in isothermal conditions, Energy 214 (2021) 118965.
[3] M. Ismail, Experimental and numerical analysis of heat sink using various patterns of cylindrical pin-fins, International Journal of Thermofluids (2024) 100737.
[4] S. Landini, T.S. O'Donovan, Experimental investigation of lithium-ion cells ageing under isothermal conditions for optimal lifetime performance, J. Energy Storage. 48 (2022) 103680.
[5] S. Arun, R.J. Boche, P. Nambiar, P. Ekka, P. Panalkar, V. Kumar, A. Roy, S. Landini, Numerical and experimental investigation on performance of thermal energy storage integrated micro-cold storage unit, Appl. Sci. 14 (12) (2024) 5166.
[6] S. Babu Sanker, R. Baby, Phase change material based thermal management of lithium ion batteries: a review on thermal performance of various thermal conductivity enhancers, J. Storage Mater. 50 (2022).
[7] J. Luo, D. Zou, Y. Wang, S. Wang, L.i. Huang, Battery thermal management systems (BTMs) based on phase change material (PCM): a comprehensive review, Chem. Eng. J. 430 (2022).
[8] P.H. Biwole, D. Groulx, F. Souayfane, T. Chiu, Influence of fin size and distribution on solid-liquid phase change in a rectangular enclosure, Int. J. Therm. Sci. 124 (2018) 433–446.
[9] J. Du, D. Bai, X. Meng, F. Jiao, Y. Hong, Effect of Cantor fractal fin arrangements on the thermal performance of a photovoltaic-phase change material system: an experimental study, Int. J. Heat Mass Transf. 219 (2024).
[10] D. Groulx, P.H. Biwole, M.h. Bhouri, Phase change heat transfer in a rectangular enclosure as a function of inclination and fin placement, Int. J. Therm. Sci. 151 (2020).
[11] J. Jiang, Y. Hong, Q. Li, D. Juan, Evaluating the impacts of fin structures and fin counts on photovoltaic panels integrated with phase change material, Energy 283 (2023).

[12] Q. Li, J. Jiang, Y. Hong, D. Juan, Numerical investigation of thermal management performances in a solar photovoltaic system by using the phase change material coupled with bifurcated fractal fins, J. Storage Mater. 56 (2022).
[13] A. Daneh-Dezfuli, A.H. Pordanjani, Investigation of passive method in thermal management of lithium-ion batteries at different discharge rates by changing the number of cavities containing phase change materials, J. Storage Mater. 52 (2022).
[14] H. Chen, A. Abidi, A.K. Hussein, O. Younis, M. Degani, B. Heidarshenas, Investigation of the use of extended surfaces in paraffin wax phase change material in thermal management of a cylindrical lithium-ion battery: applicable in the aerospace industry, J. Storage Mater. 45 (2022).
[15] R. Fan, N. Zheng, Z. Sun, Evaluation of fin intensified phase change material systems for thermal management of Li-ion battery modules, Int. J. Heat Mass Transf. 166 (2021).
[16] A. Verma, D. Rakshit, Performance analysis of PCM-fin combination for heat abatement of Li-ion battery pack in electric vehicles at high ambient temperature, Therm. Sci. Eng. Prog. 32 (2022).
[17] G. Chen, Y. Shi, Y. Yue, A thermal management design using phase change material in embedded finned shells for lithium-ion batteries, Int. J. Heat Mass Transf. 229 (2024).
[18] H. Dey, S. Pati, P.R. Randive, L. Baranyi, Effect of finned networks on PCM based battery thermal management system for cylindrical Li-ion batteries. Case Studies, Therm. Eng. 59 (2024).
[19] B. Sazvar, H. Moqtaderi, A numerical study on the capacity improvement of cylindrical battery cooling systems using nano-enhanced phase change material and axisymmetric stepped fins, J. Storage Mater. 62 (2023).
[20] T. Dagdevir, Y. Ding, Numerical investigation of battery thermal management by using helical fin and composite phase change material, J. Storage Mater. 75 (2024).
[21] Y. Hong, D. Bai, Y. Huang, D. Juan, Effect of T-shaped fin arrangements on the temperature control performance of a phase change material heat sink, Int. Commun. Heat Mass Transfer 148 (2023).
[22] F. Zhang, L. Fu, B. Liang, Y. Zhu, H. Gou, K. Xiao, Y. He, Thermal performance analysis of a new type of branch-fin enhanced battery thermal management PCM module, Renew. Energy 206 (2023) 1049–1063.
[23] X. Chen, J. Shen, X. Xiaobin, X. Wang, S. Yanghan, J. Qian, F. Zhou, Performance of thermal management system for cylindrical battery containing bionic spiral fin wrapped with phase change material and embedded in liquid cooling plate, Renew. Energy 223 (2024).
[24] V.G. Choudhari, A.S. Dhoble, S. Panchal, M. Fowler, R. Fraser, Numerical investigation on thermal behaviour of 5 × 5 cell configured battery pack using phase change material and fin structure layout, J. Storage Mater. 43 (2021).
[25] A. Verma, P. Saikia, D. Rakshit, Unification of intensive and extensive properties of the passive cooling system under a single envelope for the thermal management of Li-ion batteries, J. Storage Mater. 50 (2022).
[26] S. Ahmad, Y. Liu, S. Ali Khan, M. Hao, X. Huang, Hybrid battery thermal management by coupling fin intensified phase change material with air cooling, J. Storage Mater. 64 (2023).
[27] M.A. Alghassab, Investigating the performance improvement of lithium-ion battery cooling process using copper fins and phase change materials (PCMs), Case Studies Therm. Eng. 59 (2024).
[28] C. Suresh, S.K. Saha, Comparative study of performance enhancement of latent thermal energy storage system with copper porous fin, J. Storage Mater. 72 (2023).
[29] Kim, Se Hyun, Seong Hyun Park, Sudhanshu Pandey, and Man Yeong Ha, *Effects of fin positioning on the thermal performance of a phase change material–filled heat sink with horizontal fins.* Journal of Energy Storage. 2023 **68**.
[30] J.R. Patel, M.K. Rathod, Phase change material selection using simulation-oriented optimization to improve the thermal performance of lithium-ion battery, J. Storage Mater. 49 (2022).
[31] A.R. Bais, D.G. Subhedhar, N.C. Joshi, S. Panchal, Numerical investigation on thermal management system for lithium ion battery using phase change material, Mater. Today Proc. (2022).
[32] E.l. Idi, M. Moussa, M. Karkri, M.A. Tankari, A passive thermal management system of Li-ion batteries using PCM composites: experimental and numerical investigations, Int. J. Heat Mass Transf. 169 (2021).
[33] R. Akula, C. Balaji, Thermal management of 18650 Li-ion battery using novel fins–PCM–EG composite heat sinks, Appl. Energy 316 (2022).
[34] A. Moaveni, M. Siavashi, S. Mousavi, Passive and hybrid battery thermal management system by cooling flow control, employing nano-PCM, fins, and metal foam, Energy 288 (2024).
[35] P. Zare, N. Perera, J. Lahr, R. Hasan, A novel thermal management system for cylindrical lithium-ion batteries using internal-external fin-enhanced phase change material, Appl. Therm. Eng. 238 (2024).
[36] C. Wu, C. Qiu, X. Yuan, N. Yuan, B. Zhang, Y. Li, L. Qin, H. Shi, Numerical study and optimization of battery thermal management systems (BTMS) Based on Fin-Phase change material (PCM) in variable gravity environments, Appl. Therm. Eng. 244 (2024).
[37] Z.-R. Li, G.-N. Liang, Y.-D. Ding, Q. Liao, X. Zhu, M. Cheng, Experimental study on the thermal management performance of lithium-ion battery with PCM combined with 3-D finned tube, Appl. Therm. Eng. 245 (2024).
[38] R. Akula, A. Minnikanti, C. Balaji, Pin fin-PCM composite heat sink solution for thermal management of cylindrical Li-ion battery, Appl. Therm. Eng. 248 (2024).
[39] N. Khaboshan, Hasan, F. Jaliliantabar, A.A. Abdullah, S. Panchal, A. Azarinia, Parametric investigation of battery thermal management system with phase change material, metal foam, and fins; utilizing CFD and ANN models, Appl. Therm. Eng. 247 (2024).
[40] S. Gungor, S. Lorente, PCM-based passive cooling solution for Li-ion battery pack, a theoretical and numerical study, Appl. Therm. Eng. 257 (2024).
[41] M.N. Khan, H.A. Dhahad, S. Alamri, A.E. Anqi, K. Sharma, S. Mehrez, A. Mohamed, Shamseldin, B. Fareed Ibrahim, Air cooled lithium-ion battery with cylindrical cell in phase change material filled cavity of different shapes, J. Storage Mater. 50 (2022).
[42] A.R. Bais, D.G. Subhedar, S. Panchal, Critical thickness of nano-enhanced RT-42 paraffin based battery thermal management system for electric vehicles: a numerical study, J. Storage Mater. 52 (2022).
[43] T. Amalesh, N. Lakshmi Narasimhan, Liquid cooling vs hybrid cooling for fast charging lithium-ion batteries: a comparative numerical study, Appl. Therm. Eng. 208 (2022).
[44] Q. Xin, J. Xiao, T. Yang, H. Zhang, X.i. Long, Thermal management of lithium-ion batteries under high ambient temperature and rapid discharging using composite PCM and liquid cooling, Appl. Therm. Eng. 210 (2022).
[45] W. Zhu, F. Lei, H. Zhong, X. Jiang, Thermal performance revival of composite PCM for hybrid BTMSs by architecture and formula integrated optimization, Appl. Therm. Eng. 210 (2022).
[46] S. Mousavi, M. Siavashi, A. Zadehkabir, A new design for hybrid cooling of Li-ion battery pack utilizing PCM and mini channel cold plates, Appl. Therm. Eng. 197 (2021).
[47] A.G. Mohammed, K.E. Elfeky, Q. Wang, Thermal management evaluation of Li-ion battery employing multiple phase change materials integrated thin heat sinks for hybrid electric vehicles, J. Power Sources 516 (2021).
[48] S. Landini, R. Waser, A. Stamatiou, R. Ravotti, J. Worlitschek, T.S. O'Donovan, Passive cooling of Li-Ion cells with direct-metal-laser-sintered aluminium heat exchangers filled with phase change materials, Appl. Therm. Eng. 173 (2020).
[49] S. Talukdar, H.M.M. Afroz, M.A. Hossain, M.A. Aziz, M.M. Hossain, Heat transfer enhancement of charging and discharging of phase change materials and size optimization of a latent thermal energy storage system for solar cold storage application, J. Storage Mater. 24 (2019) 100797.
[50] M. Ismail, A.H. Alkhazaleh, J. Masri, A. Masoud Ali, M. Ali, Experimental and numerical analysis of paraffin waxes during solidification inside spherical capsules, Therm. Sci. Eng. Prog. 26 (2021) 101095.
[51] Fluent, ANSYS, *Fluent 15 users guide.* Lebanon, USA, 2016.
[52] S. Landini, W. Delgado-Diaz, R. Ravotti, R. Waser, J. Worlitschek, A. Stamatiou, T. S. O'Donovan, Effect of geometry and thermal mass of Direct-Metal-Laser-Sintered aluminium Heat Exchangers filled with phase change materials on Lithium-Ion cells' passive cooling, Appl. Therm. Eng. 195 (2021) 117151.